AGU PUBLICATIONS

JGR

Journal of Geophysical Research: Space Physics

RESEARCH ARTICLE
10.1002/2013JA019567

Key Points:
- Agreement of Mercury plasma pressure from plasma and field observations
- Pressure enhancements observed near the planet and at the magnetopause flanks
- The pressure distributions show dawn-dusk and north-south asymmetries

Correspondence to:
H. Korth,
haje.korth@jhuapl.edu

Citation:
Korth, H., B. J. Anderson, D. J. Gershman, J. M. Raines, J. A. Slavin, T. H. Zurbuchen, S. C. Solomon, and R. L. McNutt Jr. (2014), Plasma distribution in Mercury's magnetosphere derived from MESSENGER Magnetometer and Fast Imaging Plasma Spectrometer observations, *J. Geophys. Res. Space Physics*, *119*, 2917–2932, doi:10.1002/2013JA019567.

Received 24 OCT 2013
Accepted 12 MAR 2014
Accepted article online 20 MAR 2014
Published online 25 APR 2014

Plasma distribution in Mercury's magnetosphere derived from MESSENGER Magnetometer and Fast Imaging Plasma Spectrometer observations

Haje Korth[1], Brian J. Anderson[1], Daniel J. Gershman[2,3], Jim M. Raines[2], James A. Slavin[2], Thomas H. Zurbuchen[2], Sean C. Solomon[4,5], and Ralph L. McNutt Jr.[1]

[1]The Johns Hopkins University Applied Physics Laboratory, Laurel, Maryland, USA, [2]Department of Atmospheric, Oceanic and Space Sciences, University of Michigan, Ann Arbor, Michigan, USA, [3]Geospace Physics Laboratory, NASA Goddard Space Flight Center, Greenbelt, Maryland, USA, [4]Department of Terrestrial Magnetism, Carnegie Institution of Washington, Washington, D.C., USA, [5]Lamont-Doherty Earth Observatory, Columbia University, Palisades, New York, USA

Abstract We assess the statistical spatial distribution of plasma in Mercury's magnetosphere from observations of magnetic pressure deficits and plasma characteristics by the MErcury Surface, Space ENvironment, GEochemistry, and Ranging (MESSENGER) spacecraft. The statistical distributions of proton flux and pressure were derived from 10 months of Fast Imaging Plasma Spectrometer (FIPS) observations obtained during the orbital phase of the MESSENGER mission. The Magnetometer-derived pressure distributions compare favorably with those deduced from the FIPS observations at locations where depressions in the magnetic field associated with the presence of enhanced plasma pressures are discernible in the Magnetometer data. The magnitudes of the magnetic pressure deficit and the plasma pressure agree on average, although the two measures of plasma pressure may deviate for individual events by as much as a factor of ~3. The FIPS distributions provide better statistics in regions where the plasma is more tenuous and reveal an enhanced plasma population near the magnetopause flanks resulting from direct entry of magnetosheath plasma into the low-latitude boundary layer of the magnetosphere. The plasma observations also exhibit a pronounced north-south asymmetry on the nightside, with markedly lower fluxes at low altitudes in the northern hemisphere than at higher altitudes in the south on the same field line. This asymmetry is consistent with particle loss to the southern hemisphere surface during bounce motion in Mercury's offset dipole magnetic field.

1. Introduction

Magnetometer [*Anderson et al.*, 2007] observations by the MErcury Surface, Space ENvironment, GEochemistry, and Ranging (MESSENGER) spacecraft [*Solomon et al.*, 2001] have proven to be one way to characterize the plasma pressure distribution in Mercury's magnetosphere. The diamagnetic character of plasmas requires a correspondence between plasma pressure and a decrease in magnetic pressure, $p_B = B^2/2\mu_0$, where B is the magnetic field magnitude and μ_0 is the magnetic permeability of free space. A localized plasma pressure is evident by a depression of the magnetic field. Diamagnetic depressions are frequently observed in the MESSENGER Magnetometer (MAG) data within Mercury's magnetosphere and have been used to determine the distribution of enhanced magnetospheric plasma pressures [*Korth et al.*, 2011, 2012]. In this paper, we extend those earlier analyses with plasma observations.

The spatial distribution of plasma pressure is important for understanding the interactions among the solar wind, magnetosphere, and planetary surface. Plasma enhancements near the magnetopause indicate where solar wind plasma enters the magnetosphere via magnetic reconnection [*Parker*, 1957; *Petschek*, 1964], diffusion [*Eastman et al.*, 1985], and turbulent mixing [*Axford*, 1964] processes. Magnetic reconnection occurs both at the dayside magnetopause, where interplanetary and planetary magnetic field lines merge and are subsequently swept anti-sunward by the solar wind, and in the magnetotail, where open field lines connected to the northern and southern magnetic poles reconnect pairwise and cycle back toward the dayside [*Dungey*, 1961]. In the process, solar wind plasma on interplanetary magnetic field lines is introduced to field lines rooted in the planet, via both convection and accelerated flows from dayside reconnection. Because Mercury's internal magnetic field is weak—the dipole moment is 190 nT R_M^3 [*Anderson et al.*, 2012] and the

subsolar magnetopause stands off the solar wind at a distance of, on average, only 0.45 R_M from the surface [*Winslow et al.*, 2013], where R_M is Mercury's radius or 2440 km—it has been proposed that reconnection at the dayside magnetopause may erode the subsolar magnetosphere and allow direct access of solar wind particles to the planetary surface [*Slavin et al.*, 2007]. Although MESSENGER has not observed the cusp at the subsolar magnetosphere [*Winslow et al.*, 2012], corresponding to a fully eroded magnetosphere, there is plentiful evidence for reconnection through frequent loading and unloading of the magnetic tail on ~2 min timescales, commensurate with that for the Dungey cycle [*Slavin et al.*, 2010a]. The occurrence and rate of reconnection can be inferred from observations of flux transfer events (FTEs), which have been detected at the equatorial magnetopause under both northward and southward interplanetary magnetic field during the first and second Mercury flybys [*Slavin et al.*, 2010b], in the magnetotail lobes [*Slavin et al.*, 2012], and in the dayside magnetosphere [*Imber et al.*, 2013]. Statistical analysis by *Imber et al.* [2013] showed that FTEs alone account for ~30% of the total magnetic flux transfer and are thus a major contributor to plasma entry into the magnetosphere.

In addition to reconnection, plasma can enter the magnetosphere through turbulent mixing, and Kelvin-Helmholtz (KH) waves have been observed at Mercury's magnetopause [*Boardsen et al.*, 2010; *Sundberg et al.*, 2010, 2011]. KH waves arise at the magnetopause from the velocity shear between the anti-sunward solar wind flow and the sunward motion of plasma inside the magnetosphere. It has been suggested that the finite ion gyroradius affects the growth rate of the KH instability [*Nagano*, 1979]. On the dawnside, ion gyration correlates with the vorticity of KH waves, which promotes the formation of waves and results in larger growth rates, and thus larger entry rates, than on the duskside, where ion gyration reduces the KH instability. However, *Glassmeier and Espley* [2006] predicted the duskside to be more susceptible to the KH instability, and recent particle-in-cell [*Nakamura et al.*, 2010] and kinetic hybrid simulations [*Paral and Rankin*, 2013] demonstrate that the finite gyroradius of magnetosheath ions and the direction of convection electric fields broaden the shear layer at dawn, which lowers the growth rate of the KH instability in this region. Consistent with the latter scenario, a preliminary statistical study by *Sundberg et al.* [2012] identified signatures of KH waves in the Magnetometer data predominantly at dusk. Regardless of preferential occurrence, the KH instability has been reported at Mercury and is a candidate plasma-entry mechanism for Mercury's magnetosphere.

Within the magnetosphere, the plasma distribution provides insight into the transport of charged particles toward the planet and to the surface. Plasmas entering the nightside magnetosphere are transported toward the equatorial plane to form the plasma sheet and thence to the dayside by convection [*Roederer*, 1970]. Prior to the availability of extensive in situ observations, the plasma distribution within Mercury's magnetosphere had been determined from numerical modeling. Single-particle trajectory calculations by *Delcourt et al.* [2003] revealed a substantial sodium-ion population near the planet on the nightside. These workers also found that the gyroradius of these ions exceeds the length scale of magnetic field variations in most of Mercury's magnetosphere, so that sodium and other heavy ions follow nonadiabatic trajectories, the behavior of which in turn leads to chaotic pitch-angle scattering [e.g., *Büchner and Zelenyi*, 1989] and precipitation to the surface within a narrow latitude range in each hemisphere. The spatial distribution of protons had been inferred with kinetic hybrid simulations [*Trávníček et al.*, 2007]. These simulations suggested that, under idealized conditions, protons can form a closed equatorial belt around the planet.

Mapping of plasma pressure enhancements inferred from localized depressions in the magnetic field magnitude to the magnetic equatorial plane revealed a large-scale plasma population near the planet in the portion of the nightside magnetosphere corresponding to the plasma sheet [*Korth et al.*, 2011]. This population is present within a half torus that extends from dusk to dawn at radial distances between 1 and 2.5 R_M from the dipole axis and symmetrically about the magnetic equator and displays an inward radial pressure gradient [*Korth et al.*, 2012]. The crosstail current sheet is embedded in the plasma sheet, and rotations in the magnetic field observed by the MESSENGER Magnetometer indicate that it is ~0.2 R_M thick [*Johnson et al.*, 2012]. Near the planet, the plasma sheet extends along magnetic field lines to low altitudes at mid-latitudes, where charged particles precipitate and contribute to space weathering of the planetary surface. On the dayside, plasma associated with the northern magnetospheric cusp has been observed [*Korth et al.*, 2011, 2012; *Zurbuchen et al.*, 2011; *Raines et al.*, 2013]. Cusp plasma has direct access to the surface, and the northern cusp has a mean extent of ~11° in latitude and 4.5 h in local time [*Winslow et al.*, 2012]. The area of the southern hemisphere cusp, which cannot be observed by MESSENGER because of the eccentricity and

high northern periapsis of the spacecraft's orbit, is estimated to be ~4 times larger because of the northward offset of the internal dipolar field [*Winslow et al.*, 2012], and the flux to the surface is correspondingly higher. The northern cusp population has also been shown to be dynamic, exhibiting plasma pressures for anti-sunward orientation of the interplanetary magnetic field (IMF) to be 40% higher than for sunward orientation [*Winslow et al.*, 2012]. In summary, mapping the plasma distribution inside the magnetosphere yields indirect insight into a range of interaction processes among the solar wind, Mercury's magnetic field, and the planetary surface.

Knowledge of the plasma distribution also contributes to determination of the planetary magnetic field. The location of the plasma sheet at the magnetic equator provides independent confirmation of the substantial, ~480 km, northward offset of the internal dipole [*Anderson et al.*, 2011, 2012]. The plasma sheet thickness can constrain the thickness of the crosstail current sheet [*Johnson et al.*, 2012] in global magnetospheric magnetic field models [e.g., *Alexeev et al.*, 2010]. The effects of plasma pressure on the locally measured magnetic field must be considered in determinations of higher-order moments of the planetary magnetic field. Estimates for the quadrupole term and upper limits on higher-order moments, expressed as Gauss coefficients for the axially aligned terms of degrees $l = 2$, 3, and 4 obtained by *Anderson et al.* [2012], were $g_{20} = -75$ nT, $|g_{30}| < 22$ nT, and $|g_{40}| < 6$ nT. At the magnetic equator, where plasma is most abundant in the nightside magnetosphere, the magnitude of the quadrupole term is

$$B_q = \frac{3}{2}\left(\frac{R_M}{r}\right)^4 g_{20}, \tag{1}$$

where r is the radial distance. Magnetic depressions in excess of 50 nT have been observed at ~1.2 R_M radial distance from the internal dipole [*Korth et al.*, 2011, 2012], whereas the quadrupole field at this distance is 54 nT, comparable to or smaller than the diamagnetic depressions of the magnetic field. The higher-order fields are smaller than the quadrupole and fall off more quickly with increasing distance and thus yield signatures at MESSENGER altitudes that are lower than many magnetic depressions. Reliable estimates of the higher-order structure in Mercury's magnetic field must therefore account for the effects of the plasma on the magnetic field measurements.

The paper is organized as follows. In section 2, we describe a modification to the magnetic field model used for tracing the observations to eliminate mapping artifacts in the equatorial distributions. Analysis of plasma data and their spatial distributions are described and compared with those inferred from magnetic pressure deficits in section 3. The results are discussed in section 4 and summarized in section 5.

2. Magnetic Field-Line Mapping

2.1. Magnetospheric Equator

The statistical plasma distribution in Mercury's magnetosphere was previously inferred from mapping the magnetic pressure deficits observed from orbit over an ~11 month period along the magnetic lines of force to both the magnetic equatorial plane and to low altitudes [*Korth et al.*, 2012]. This mapping technique requires that the plasma pressure be isotropic, which implies that the pressure is constant along the magnetic field line [*Spence et al.*, 1989; *Goertz and Baumjohann*, 1991]. The global magnetic field needed for the mapping process was provided by the *Alexeev et al.* [2010] magnetic field model, which includes the planetary field represented by a spin-axis-aligned, southward-directed dipole of moment 190 nT R_M^3 and a 479 km offset northward along the spin axis [*Anderson et al.*, 2011, 2012; *Johnson et al.*, 2012] and external contributions to the magnetic field generated by magnetopause and magnetotail currents. The best-fit parameters for the *Alexeev et al.* [2010] model, which minimize the residuals with respect to the magnetic field observations, were determined by *Johnson et al.* [2012]: the magnetopause subsolar stand-off distance from the internal dipole is $R_{SS} = 1.45\ R_M$; the half-thickness of the cross-tail current sheet is 0.09 R_M; the distance from the planet surface to the inner edge of the cross-tail current sheet is $R_2 = 1.41\ R_M$; the magnetotail field intensity is $B_T = 137$ nT; and the paraboloid flaring parameter is $\gamma = 1$. Unfortunately, this parameterization yields unphysical magnetic islands (O-type magnetic field lines, or O-lines, which close on themselves) in the model at the dawn and dusk flanks of the magnetosphere near the planet, attributable to an overly sharp inner edge of the tail current sheet. These portions appear as white patches in regions of the equatorial plane not accessible by field lines traversed by the MESSENGER spacecraft [cf. *Korth et al.*, 2012,

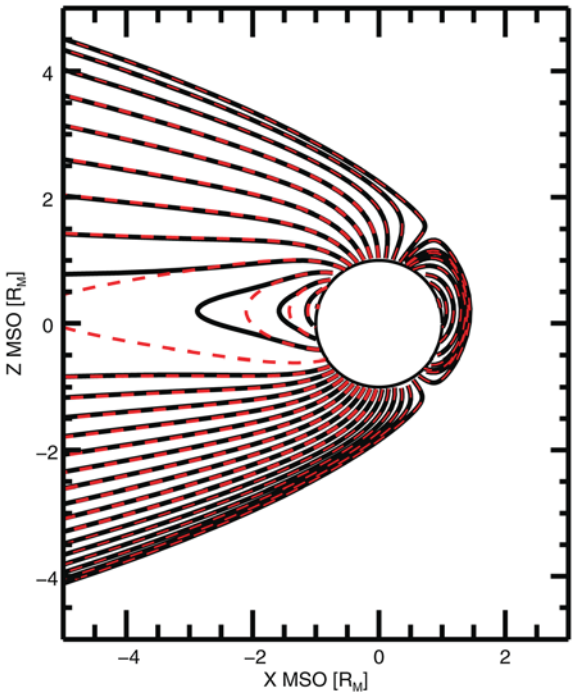

Figure 1. Comparison of the best-fit (solid black lines) and modified (dashed red lines) model [*Alexeev et al.*, 2010] magnetic field lines in the MSO *X-Z* plane at $Y = 0$. The half-thickness of the crosstail current sheet for these models is 0.09 R_M and 0.75 R_M, respectively. The circle outlines Mercury's surface, and the Sun is to the right.

Figures 9–11]. Eliminating O-lines in the model required an eightfold increase in the half-thickness of the current sheet, from 0.09 R_M to 0.75 R_M, and this modified model is used to compute a revised equatorial map. To quantify the corresponding change in the mapping, Figure 1 compares the magnetic field lines of the best-fit model (solid black lines) and the modified model with increased current-sheet thickness (dashed red lines) in the noon-midnight meridian of the Mercury solar orbital (MSO) coordinate system, where $+X$ is toward the Sun, $+Y$ is duskward, $+Z$ is northward, and the origin coincides with the planet center. Both parameterizations yield similar field line geometry except near the nightside equatorial plane, where the closed field lines of the modified model map somewhat closer to the planet.

An estimate of the mapping uncertainty was obtained by mapping magnetic field lines originating at the planetary surface to the magnetic equatorial plane and comparing the equatorial crossing points between the two models. Figure 2 shows the dependence of the equatorial mapping distance on the Mercury solar magnetospheric (MSM) latitude of field lines originating on the planetary surface at local midnight for the best-fit (solid line) and modified (dashed line) *Alexeev et al.* [2010] models. MSM coordinates are centered on the planetary dipole and correspond to MSO coordinates displaced 479 km to the north [e.g., *Korth et al.*, 2011]. At low latitudes, the field lines of surface locations that increase in latitude map to increasingly distant locations in the equatorial plane. Toward mid-latitudes, the equatorial mapping point approaches asymptotically the latitude of the boundary between open and closed field lines. The mapping uncertainty associated with the modification of the *Alexeev et al.* [2010] model can be estimated from the difference in the open-closed boundary between the two models and is ~7° in latitude. Similarly, the equatorial mapping uncertainty for surface locations at a given latitude can be estimated from the vertical difference between the two curves in Figure 2. This uncertainty increases with latitude and amounts from <0.5 R_M for latitudes $\leq 30°$ to ~3 R_M at the open-closed boundary of the best fit model. For altitudes above the surface, the equatorial mapping uncertainty becomes smaller, so that the estimates inferred from Figure 2 are upper limits. Furthermore, because the tail current sheet

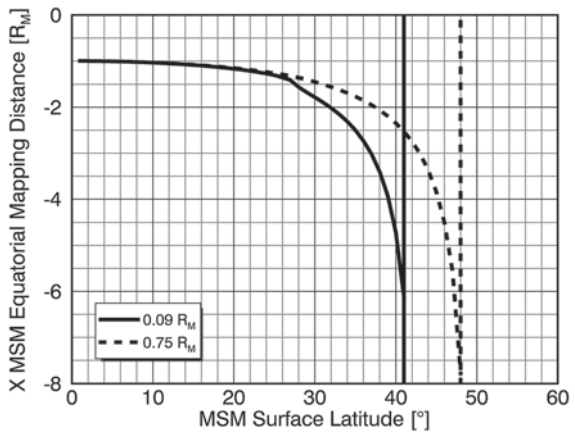

Figure 2. Dependence of the equatorial mapping distance on the MSM latitude of field lines originating on the planetary surface at local midnight for the best-fit (solid line) and modified (dashed line) *Alexeev et al.* [2010] models, labeled by the half-thickness of the cross-tail current sheet. The asymptotic vertical lines indicate the latitudes of the boundary between open and closed magnetic field lines.

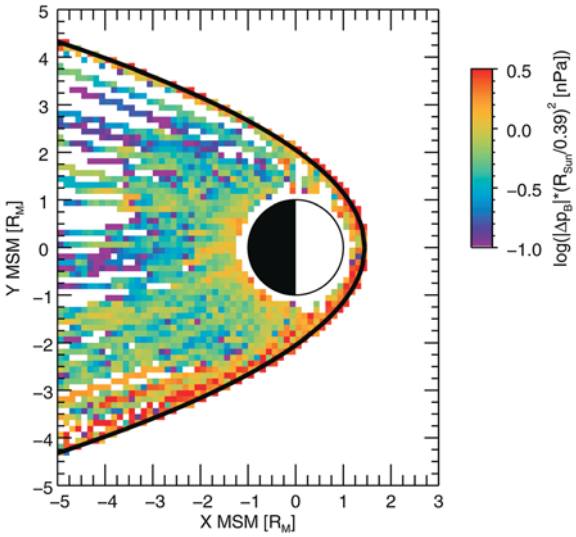

Figure 3. Distribution of the mean magnetic pressure deficit mapped to Mercury's magnetic equatorial plane and normalized to a heliocentric distance of 0.39 AU. Observations were mapped with the modified *Alexeev et al.* [2010] model and a half-thickness of the cross-tail current sheet of 0.75 R_M. The circle denotes the planet, the Sun is to the right, and the magnetopause of the magnetic field model is represented by the solid black line.

is restricted to the nightside magnetosphere, the latitude difference between the open-closed boundaries of the best-fit and modified models, and thus the equatorial mapping uncertainty, decreases toward the dayside and vanishes near local noon.

With the modified *Alexeev et al.* [2010] magnetic field model, we then remapped the equatorial magnetic pressure distribution [cf. *Korth et al.*, 2012, Figure 9]. The revised distribution is shown in Figure 3 for a larger section of the magnetic equatorial plane than presented in the previous study. To account for seasonal variations in the solar wind environment resulting from the large eccentricity of Mercury's orbit about the Sun, all pressures were normalized to Mercury's mean heliocentric distance, 0.39 AU, with the scale factor $(r_s/0.39)^2$, where r_s is Mercury's heliocentric distance in AU at the time of observation [*Korth et al.*, 2012]. The voids at the dawn and dusk flanks are no longer present, whereas the dominant features in the equatorial pressure distribution, including the nightside enhancement near the planet and the inward radial pressure gradient, are qualitatively preserved. At larger distances, especially on the duskside, the distribution becomes patchy where bins are not threaded by field lines on which magnetic depressions were observed. The revised distribution in Figure 3 is used below for comparison with the plasma observations.

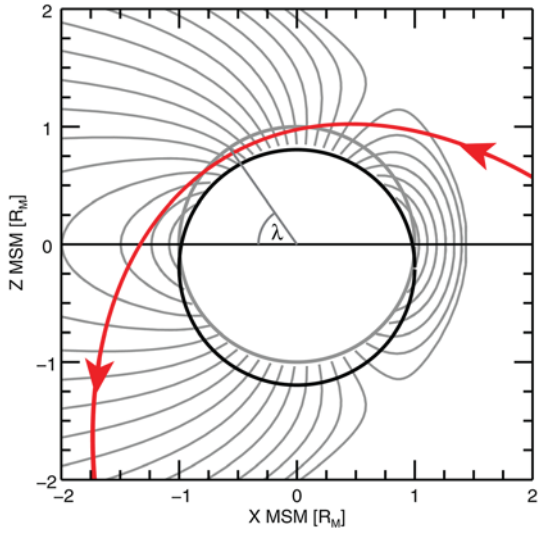

Figure 4. Illustration of the mapping procedure to identify the invariant latitude, λ. Shown in the MSM *X-Z* plane at $Y = 0$ are the planetary surface and the 1 R_M sphere in MSM coordinates (black and grey circles, respectively), magnetic field lines (grey), and the MESSENGER trajectory in this noon-midnight plane (red, with arrows indicating the direction of spacecraft motion).

2.2. Invariant Latitude

In addition to the equatorial distribution, the inferred plasma pressures have been mapped to low altitudes. To preserve the geometry of the field lines on which observations were made, the observations were mapped onto a grid of invariant latitude and local time. The invariant latitude, λ, is the latitude at which the field line threading the observing location maps onto a sphere of radius 1 R_M centered on the offset dipole moment, as illustrated in Figure 4. The invariant latitude was obtained by tracing the magnetic field line threading the spacecraft location to the 1 R_M MSM sphere in the respective hemisphere with the modified *Alexeev et al.* [2010] magnetic field model. Organizing the observations by invariant latitude rather than planetocentric latitude facilitates critical examination of asymmetries of the low-altitude plasma distribution with respect to the magnetic equator.

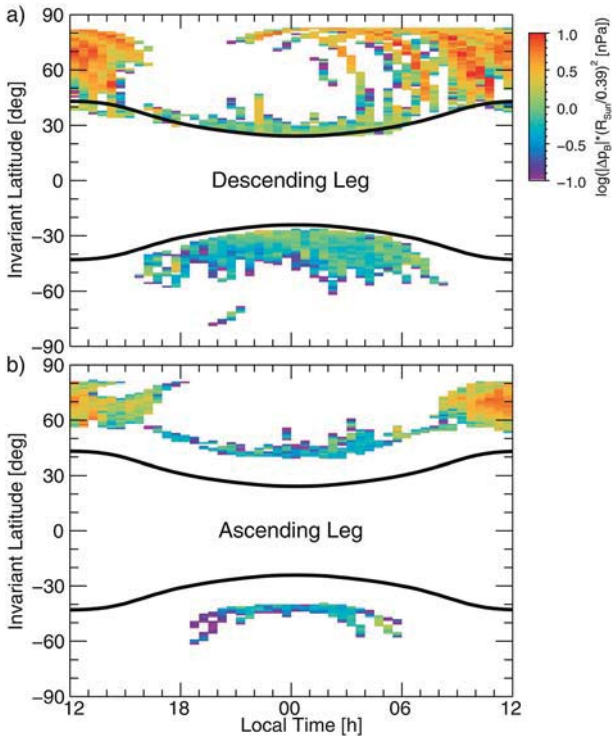

Figure 5. Distribution of the mean magnetic pressure deficits with respect to invariant latitude and local time observed on the (a) descending and (b) ascending legs of each orbit. The observations were normalized to a heliocentric distance of 0.39 AU. The black lines confine the region of closed model field lines near the equator not sampled by MESSENGER.

The low-altitude distribution of the magnetic pressure deficit as a function of invariant latitude and local time is shown in Figure 5, in which observations on the descending (Figure 5a) and ascending (Figure 5b) orbit segments are shown separately. The equatorial gap in λ (delimited by black lines in Figure 5) corresponds to field lines that are not intersected by the MESSENGER orbit. Both panels of the figure show a persistent plasma population associated with the high-latitude dayside cusp region. Observations on the descending orbit leg are obtained at lower altitudes than for the ascending orbit leg and, hence, extend to lower $|\lambda|$ than those on the ascending leg. The distributions for the ascending and descending leg differ most on the nightside. On the descending leg of the orbit, there is a prominent north-south asymmetry in the pressure, such that the latitude range of the pressure observations is about three times wider in the south than the north. This asymmetry is not found on the ascending leg, for which the latitude range over which the pressure deficits are observed is about equal in both hemispheres.

3. Plasma Data Analysis

Plasma observations are obtained by MESSENGER's Fast Imaging Plasma Spectrometer (FIPS), one of two sensors on the Energetic Particle and Plasma Spectrometer (EPPS) instrument [*Andrews et al.*, 2007]. FIPS combines a time-of-flight detector with an electrostatic analyzer to measure the mass per charge (m/q) and energy per charge (E/q) ratios of incident ions. The instrument has a simultaneous 1.4π sr field of view, which is reduced to 1.15π sr by obstructions from the spacecraft, and registers incident ions with an angular resolution of ~15° [*Andrews et al.*, 2007]. We used measurements of the proton flux as function of E/q to derive estimates of the proton thermal pressure, and we employed fits to fill in unobserved portions of phase space [cf. *Gershman et al.*, 2013, and references therein] to derive average spatial distributions for comparison with the magnetic pressure deficits. Protons were detected by FIPS in 50 logarithmically spaced steps in E/q in the energy range from 100 eV/e to 13.3 keV/e with an integration time of 50 ms at each step. The observations included in the statistical analysis were obtained from 11 April 2011 to 12 February 2012, which differs from that studied by *Korth et al.* [2012] (23 March 2011 to 12 February 2012) by about 2 weeks, owing to differences in the completion date of commissioning of the MAG and EPPS instruments for the Mercury orbital phase of the MESSENGER mission. We restricted the data set to observations obtained within the magnetosphere, which is identified from the MAG data as the interval between the innermost inbound and outbound magnetopause crossings [*Winslow et al.*, 2013]. The same normalization for heliocentric distance used for the magnetic pressure deficit analysis was applied to the proton counts and thermal pressure estimates.

3.1. Proton Flux Distributions

The equatorial distribution of the proton flux was calculated by selecting observations on closed model magnetic field lines, mapping them to the magnetic equator, and averaging them in bins of dimensions $0.125 \times 0.125\ R_M$. The resulting distribution in the MSM X-Y plane at $Z = 0\ R_M$ is shown in Figure 6. The

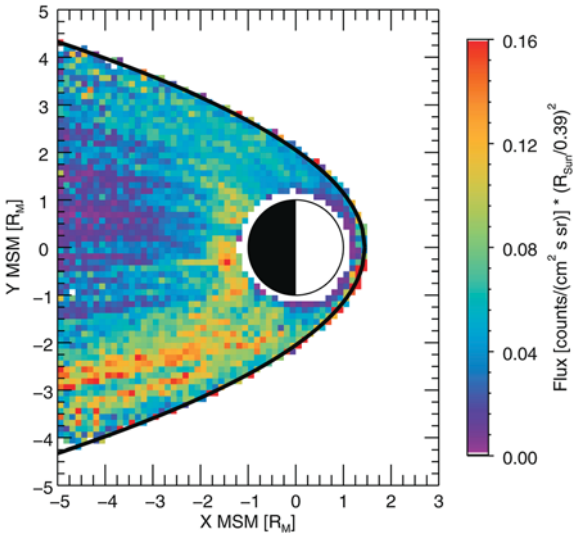

Figure 6. Distribution of the mean proton flux mapped to Mercury's magnetic equatorial plane and normalized to a heliocentric distance of 0.39 AU. The circle denotes the planet, the Sun is to the right, and the magnetopause of the magnetic field model is represented by the solid black line.

enhanced plasma population observed in a toroidal section extending near the planet nightside from dusk to dawn is similar to that inferred from the magnetic pressure distribution (cf. Figure 3). The low flux levels on the dayside confirm that the plasma population is tenuous in this region, supporting the hypothesis that protons in the energy range measured by FIPS typically do not complete their drift orbits around the planet as they do at Earth [*Ness*, 1979; *Russell et al.*, 1988; *Korth et al.*, 2012]. Note that the increase in plasma pressure at the dayside magnetopause inferred from the Magnetometer data was shown to be due to cusp pressure observations having erroneously been identified as located on closed field lines in the model. In contrast to the plasma distribution inferred from Magnetometer data, Figure 6 also shows increases in the proton flux levels at magnetopause flanks, which are stronger at dawn than at dusk. These enhancements are less pronounced in the magnetic pressure distributions because the event count is smaller.

To illustrate that the features evident in the statistical analysis correspond to structures observed on individual orbits, FIPS proton and Magnetometer data are shown for four representative magnetospheric transits in Figure 7. The innermost inbound and outbound magnetopause boundaries are indicated by the vertical dashed lines. In Figure 7c, the proton spectrogram changes near 2100 UTC, when the FIPS instrument transitioned to a scan mode with lower time resolution and lower minimum energy. Figures 7a and 7b show data from orbits with spacecraft motion from dawn to dusk and dusk to dawn, respectively. During both orbits, enhanced proton fluxes were evident at the dawnside and duskside magnetopause flanks adjacent to the magnetopause, which is unambiguously identified by a rotation in the magnetic field azimuth angle and a change in the amplitude of magnetic fluctuations. In addition, the magnetopause distinctly separated the more energetic protons observed at the magnetosphere flanks from the colder magnetosheath population. For both cases in Figures 7a and 7b, the count rates at dawn were substantially higher than those at dusk, consistent with the statistical dawn-dusk asymmetry and indicating that the asymmetry is at least partially free of bias in the observations with respect to the Mercury's orbit phase. The flank populations were not previously identified in the Magnetometer observations. Comparison of depressions in the magnetic field magnitude associated with the flank populations (Figure 7, top panels) with those observed in the plasma sheet and cusp [*Korth et al.*, 2011, 2012] shows that the former are small compared with the latter and occur over extended periods of time so they are difficult to identify reliably in the Magnetometer data.

Observations during magnetosphere transits with the spacecraft moving in midnight-to-noon and noon-to-midnight directions are shown in Figures 7c and 7d, respectively. The key features observed in these orbits are as follows. The flux levels are low on the dayside equatorward of the cusp, 2007 to 2015 UTC on orbit 205 and 2214 to 2229 UTC on orbit 500, demonstrating that few particles complete their drift around the planet dayside. The fluxes are also low at middle to high latitudes, 2021 to 2031 UTC (northern hemisphere) and 2052 to 2129 UTC (southern hemisphere) on orbit 205 and 2030 to 2107 UTC (southern hemisphere) and 2202 to 2207 UTC (northern hemisphere) on orbit 500, corresponding to the region that is magnetically connected to the center-tail minimum observed between the flank populations in Figure 6. As the spacecraft crossed the magnetic equator near midnight, there was a dropout in the proton fluxes north of the equator, from 2033 to 2038 on orbit 205 and from 2140 to 2145 on orbit 500.

The low-altitude mapped distribution of the proton flux is obtained in the same manner as that for the magnetic pressure deficit by binning the observations with respect to magnetic local time and invariant

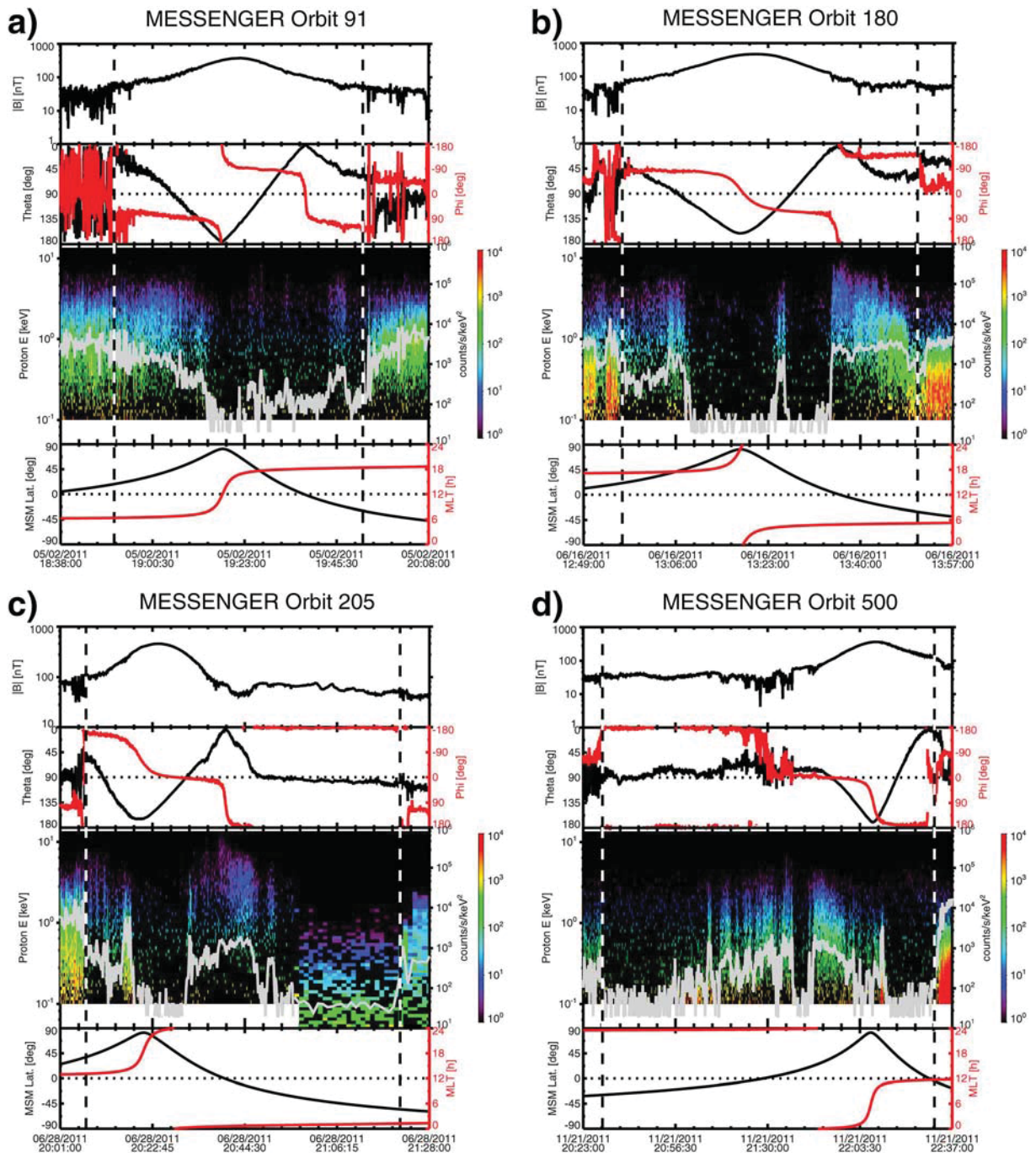

Figure 7. Magnetic field and plasma observations during magnetosphere transits for the orbits indicated at the top of each panel. From top to bottom, each panel shows the magnetic field magnitude; the magnetic field polar (black) and azimuth (red) angles; the proton flux spectrogram color-coded by count rate and over-plotted in grey with the total count rate; and the spacecraft MSM latitude (black) and local time (red). The innermost magnetopause boundaries are indicated by vertical dashed lines. The panels show sample orbits with the ascending orbit leg in the (a) dawn-to-dusk, (b) dusk-to-dawn, (c) noon-to-midnight, and (d) midnight-to-noon directions.

latitude as described in section 2.2. The distributions for the descending and ascending orbit leg observations are shown in Figures 8a and 8b, respectively. Each panel shows the mean proton flux color-coded by magnitude in bins of dimensions 0.5 h in magnetic local time and 1° in invariant latitude. The heavy black lines in both panels show the mean λ closest to $\lambda = 0°$ sampled on the descending orbit leg. The equatorial

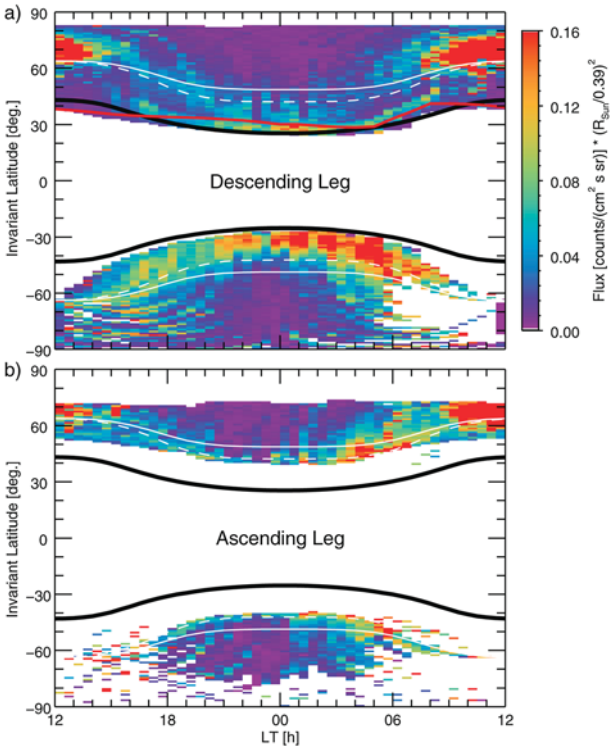

Figure 8. Distribution of the mean proton flux with respect to invariant latitude and local time observed on the (a) descending and (b) ascending legs of each orbit. The observations were normalized to a heliocentric distance of 0.39 AU. The black lines confine the region of closed model field lines near the equator not sampled by MESSENGER. The boundaries between open and closed field lines in the best-fit and modified *Alexeev et al.* [2010] magnetic field model are represented by white dashed and solid lines, respectively. The red line in Figure 8a depicts the loss boundary.

edge of the distributions corresponds to the minimum $|\lambda|$ sampled at that local time, that is, the magnetic equator. The white and red traces in the figure are discussed in section 4.

The highest proton fluxes are observed on the nightside at middle southern latitudes and in the northern cusp on the dayside. On the ascending orbit leg, the highest fluxes are in the northern cusp. In the descending leg observations, there is a pronounced north-south asymmetry in the nightside flux distribution. The most intense nightside fluxes are observed in a substantially wider latitude range in the southern hemisphere than in the north. Whereas the southern hemisphere mid-latitude flux is uniformly distributed in latitude within ~20° in λ of the equator, in the northern hemisphere, there is a band of enhanced fluxes within ~5° of the minimum λ sampled, near the equator, and a weaker enhancement in the fluxes 15° to 20° in λ northward. As discussed below, the north-south asymmetry in the nightside descending leg observations is attributed to the northward offset of the planetary magnetic dipole.

Both the ascending and descending observations show that the fluxes at dawn are higher than at dusk, consistent with the equatorial mapping (cf. Figure 6). The dawn-dusk asymmetry is most evident in the southern hemisphere descending observations, but it is present also in the ascending orbit data in both the northern and southern hemispheres.

Finally, some flux observations map to the dayside polar region but are in fact observed at spacecraft locations tailward of the dawn-dusk terminator. These fluxes are observed in close proximity to the magnetopause on open magnetospheric field lines, which are rooted in the planet at high latitudes on the dayside and extend far into the magnetotail, as shown in Figure 1. The mapping along field lines close to the magnetopause is very sensitive to the geometry of the magnetic field and small deviations between the model and the natural system and result in large uncertainties, so the results in this region are not regarded as indicative of the low-altitude fluxes. Therefore, the southern high-latitude observations are not considered further in this study.

3.2. Proton Pressure Distributions

The FIPS instrument observes only partial distribution functions, so plasma moments, including the thermal pressure, cannot be directly computed from the observations under all conditions. However, for plasmas with subsonic flow velocities and modest temperature anisotropies, conditions that are typically encountered throughout Mercury's magnetosphere and, particularly, in the nightside plasma sheet, density, temperature, and pressure estimates can be recovered from *E/q* distributions only [*Gershman et al.*, 2013]. The above conditions are not as well satisfied in the cusp, where precipitation to the planetary surface can result in strong directional anisotropies, but FIPS observations there should nonetheless provide a reasonable first-order estimate of plasma pressure. The plasma pressures were derived from

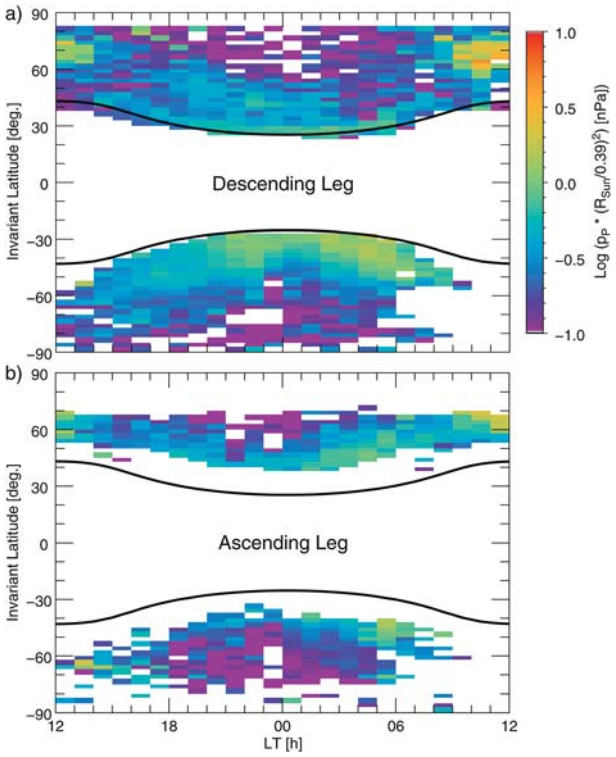

Figure 9. Distribution of the mean proton pressure with respect to invariant latitude and local time observed on the (a) descending and (b) ascending nodes of the orbit. The observations were normalized to a heliocentric distance of 0.39 AU. The black lines confine the region of closed model field lines near the equator not sampled by MESSENGER.

proton *E*/*q* distributions by application of the technique of *Gershman et al.* [2013] to data acquired over 1 min intervals within Mercury's magnetosphere during which more than 50 ion counts were recorded, summed over all energy channels. The pressure estimates are for protons only and do not account for contributions from electrons or heavy ions.

Statistical distributions of the proton pressure with respect to magnetic local time and invariant latitude were obtained in the same manner as for the distributions of magnetic pressure deficit (Figure 5) and the proton flux (Figure 8). Because of the ~1 min integration time for each pressure inversion, a larger bin size of 1 h by 2.5° was used to average the results. The average plasma pressure distributions for the descending and ascending legs of the MESSENGER orbits are shown in Figure 9. The distribution of the proton pressure is similar to that of the magnetic pressure deficit and the proton flux. The highest pressures are primarily in the plasma sheet and the cusp. Furthermore, the nightside plasma sheet pressure observed on the descending leg of each orbit is markedly higher in the south than in the north for invariant latitudes within ~20° of the magnetic equator. There is also a faint double-banded structure in the pressure on the descending leg at night in the northern hemisphere, with enhanced pressures within a few degrees of the equator and again ~20° farther poleward. The pressure distributions for both the descending and ascending orbit segments have higher pressures at dawn than at dusk.

To quantify the comparison between the FIPS proton pressure estimates and the magnetic pressure deficits, we paired each plasma pressure estimate with the average of the magnetic pressure deficit derived for the same interval. The observations of FIPS-derived proton pressure versus magnetic pressure deficit are shown in Figure 10. Figure 10a includes proton pressure observations within the magnetosphere but excluding those on the dayside northward of 45°N latitude, the region broadly associated with the northern cusp; the observations for the latter region are shown in Figure 10b. The regression coefficients for the sets of data points in Figures 10a and 10b are 0.25 and 0.48, respectively, indicating only modest correlation between the pressure estimates. From the distributions, it is evident that order of magnitude differences between

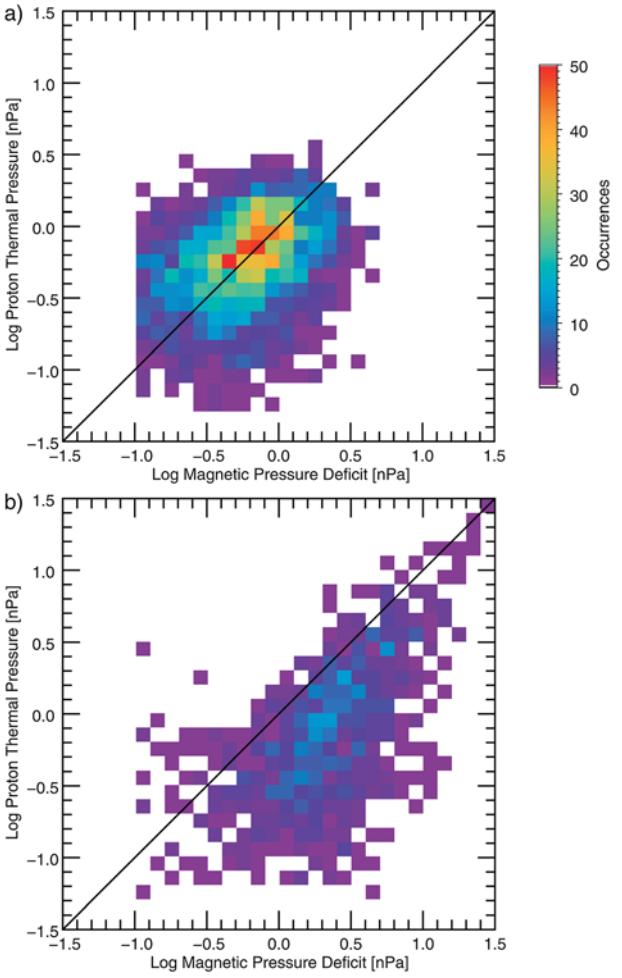

Figure 10. Proton thermal pressure versus simultaneously observed magnetic pressure deficit for (a) non-cusp and (b) cusp events. The cusp is broadly defined as the dayside region northward of 45°N latitude. The black lines indicate a slope of unity for reference.

the δp_B and p_{H+} values are not uncommon and that the dayside high-latitude observations exhibit somewhat more scatter. The distribution of data excluding the cusp peaks for $p_{H+} = \delta p_B$ and clusters within a factor of 3 of the $p_{H+} = \delta p_B$ line. The data in the cusp region distribution are biased to $p_{H+} < \delta p_B$.

4. Discussion

Statistical distributions of the proton flux and pressure derived from FIPS observations in orbit about Mercury have been compiled by averaging measurements projected along magnetic field lines both to the magnetic equatorial plane and to low altitudes. The FIPS results have also been compared with estimates of the total plasma pressure from magnetic pressure deficits. The FIPS distributions are qualitatively similar to those of the magnetic pressure deficit in regions where magnetic depressions were identifiable. In addition, the proton pressures derived from the FIPS data and the magnetic pressure deficits are in agreement on average, although substantial differences were found from case to case. We first discuss possible reasons for the scatter in the quantitative comparison of proton thermal pressure and magnetic pressure deficit results and then proceed to a consideration of the key results of the plasma distribution in Mercury's magnetosphere and the implications for plasma entry, transport, and precipitation loss to the surface.

Although the distributions of the magnetic pressure deficit and the proton thermal pressure compared well qualitatively, direct comparison of the pressures reveals only a modest correlation. The FIPS proton pressure estimates agree on average with the magnetic pressure deficits except in the cusp region, where p_{H+} is systematically low. In addition, discrepancies in the pressures of up to an order of magnitude were observed, but outside of the cusp region the differences within the magnetosphere were typically within a factor of 3. Several factors may contribute to these disparities. First, the magnetic depressions reflect a magnetic pressure deficit relative to the background pressure. If the background plasma pressure is not negligible, the magnetic pressure deficit underestimates the total plasma pressure. Second, the FIPS pressures are for protons only and do not include contributions from electrons or heavy ions. In the Earth's magnetotail plasma sheet, the proton temperature is a factor of 8 greater than the electron temperature on average [*Baumjohann et al.*, 1989]. So unless the relative dynamics forming the plasma sheet at Mercury are markedly different from those at Earth, ignoring the electron pressure should lead to a modest, 10 to 20%, underestimate of the plasma pressure. Compositional observations in Earth's plasma sheet have revealed a relative He^{2+} abundance of 3% [*Lennartsson and Shelley*, 1986; *Lennartsson*, 1992; *Fuselier et al.*, 1999], consistent with a relative abundance for these ions of 3–5% in the solar wind [*Feldman et al.*, 1978] and solar wind penetration into the magnetosphere. The temperature of He^{2+} typically exceeds that of H^+ by a factor of 4 [*Fuselier et al.*, 1997].

Thus, if the solar wind heating and acceleration processes at Mercury are comparable with those at Earth, He^{2+} may contribute as much as 10–15% to the total pressure. In addition, FIPS observations in Mercury's plasma sheet during three orbits recorded in April 2011 have shown contributions from sodium ions with pressure ratios of $p_{Na^+}/p_{H^+} = 4$–33% [*Zurbuchen et al.*, 2011]. Thus, pressures from other species could contribute up to half of the total pressure, so the FIPS proton pressures could be as much as a factor of 2 lower than δp_B for this reason. Finally, we expect that the protons in the cusp are highly anisotropic since the fluxes directed upward from the planet should be markedly depleted for pitch angles within the loss cone [cf. *Winslow et al.*, 2012]. This direction dependence violates the assumption of isotropy applied in the FIPS proton pressure inversions and would lead to an underestimate of the proton pressure [*Gershman et al.*, 2013]. It is also possible that other species contribute significantly to the plasma pressure in the cusp [cf. *Raines et al.*, 2011, 2013; *Zurbuchen et al.*, 2011]. Thus, we conclude that the systematic difference between δp_B and p_{H+} in the cusp is likely due to the character of the proton distributions, whereas the factor of 2–3 scatter elsewhere could be due to plasma composition variations so that p_{H+} underestimates the total plasma pressure, background plasma effects so that δp_B underestimates the total pressure, and uncertainties in the FIPS pressure inversions.

Nonetheless, the direct measurement of protons by FIPS provides substantially greater fidelity in the measurement of the distribution of plasma in Mercury's magnetosphere than the magnetic pressure deficits alone. Both the FIPS results and the pressure deficit analysis show strong enhancements in the northern cusp region and a plasma enhancement in a toroidal section extending at 1–2 R_M radial distance on the planet's nightside from dusk to dawn. In addition to confirming these results, however, the FIPS observations reveal features that were either difficult to discern or could not be resolved with the Magnetometer data.

The FIPS proton fluxes exhibit a pronounced dawn pressure enhancement along the magnetopause flank, a minimum in the center of the far magnetotail, and another enhancement along the dusk flank but with fluxes markedly lower than at the dawn flank (Figure 6). This feature of the plasma distribution in the tail was barely perceptible in the magnetic pressure deficit analysis. The open-closed boundary (cf. Figure 8) was computed by tracing magnetic field lines from the northern to the southern hemisphere surface and vice versa in 0.1° latitude steps for each hour in local time until either the opposite hemisphere surface was reached, corresponding to closed field lines, or the field line distance exceeded 10 R_M, at which point the field line was assumed to be open. Thus, invariant latitudes equatorward of these lines on the nightside map to the magnetotail, as shown in Figures 3 and 6. The dawn-dusk asymmetry is also prevalent in the low-altitude distributions for the southern descending leg and for the ascending leg in both the north and south (Figure 8). Recall that the proton fluxes and pressures have been scaled by $1/r_s^2$ to correct for variations in average solar wind background density with Mercury heliocentric distance. The fact that this dawn-dusk asymmetry was observed for individual cases at Mercury aphelion (Figure 7c) and perihelion (Figure 7d) indicates that the statistical result reflects an actual feature of the plasma distribution at Mercury and is not a residual artifact in the seasonal coverage provided by the MESSENGER orbit.

Plasma enhancements at magnetopause flanks have also been observed in the low-latitude boundary layer of the terrestrial magnetosphere [*Wing and Newell*, 1998], where particles from the magnetosheath can enter the magnetosphere, e.g., through turbulent mixing of the solar wind and the outer fringes of the magnetosphere resulting from the KH instability [*Axford*, 1964]. Diffusive particle entry into the magnetosphere has been observed at Earth [*Terasawa et al.*, 1997; *Fairfield et al.*, 2000], and the considerable mass transport into the magnetosphere has been linked to magnetic reconnection in KH vortices [*Otto and Fairfield*, 2000]. The observed dawn-dusk asymmetry in the proton fluxes is consistent with the hypothesis by *Nagano* [1979] that ion gyration promotes the formation of KH waves on the dawnside, leading to larger growth rates and thus larger entry rates at dawn than at dusk, where ion gyration reduces the KH instability. This hypothesis is, however, inconsistent with observations by MESSENGER [*Boardsen et al.*, 2010; *Sundberg et al.*, 2010, 2011] and particle simulations [*Nakamura et al.*, 2010; *Paral and Rankin*, 2013], which show KH waves primarily at the duskside magnetopause, where plasma enhancements should thus be stronger. The above considerations are predicated on the assumption that the seed plasma population in the magnetosheath is relatively uniform, so KH mixing introduces similar amounts of plasma at both flanks. Hybrid simulations [*Trávníček et al.*, 2010], however, have shown pronounced dawn-dusk asymmetries in the

magnetosheath plasma distribution, which depend on IMF orientation [*Herčík et al.*, 2013]. Thus, whereas the KH instability remains a possible means for diffusive plasma transport into the magnetosphere, additional analysis accounting for the magnetosheath source plasma is needed to determine definitively the importance of this mechanism over other processes.

The equatorial distribution of the proton flux (Figure 6) also shows that plasma is depleted in the dayside magnetosphere. This result is in contrast to that from the magnetic pressure deficit analysis (Figure 3), which did not resolve this feature. Indeed, as noted in the previously published analysis of the magnetic pressure deficits [*Korth et al.*, 2012], the large magnetic pressure deficits on the dayside are attributed to magnetic depressions within the magnetosheath that are erroneously mapped to the equatorial plane with the average magnetopause and magnetic field model. Note that for consistency with previous magnetic field analysis, the magnetic pressure deficit statistics were calculated from data intervals constrained by the model magnetopause because the magnetopause crossing list was not available when these analyses were first done. The FIPS analysis, however, uses the actual magnetopause crossings so that magnetosheath data are excluded by definition. Moreover, the dayside magnetosphere is sampled by MESSENGER near the planet at fairly low altitudes, where the gradient in the planetary field along the MESSENGER trajectory is high. Discerning deficits in the magnetic field against a steep gradient in the observed field is not straightforward, but the direct detection of protons by FIPS alleviates this problem. The FIPS observations are thus critical in correcting this limitation of the pressure deficit analysis, and they confirm that the plasma typically does not encircle the planet on closed drift paths, consistent with Mercury's small dipole magnetic and corotation electric fields [*Ness*, 1979; *Russell et al.*, 1988; *Slavin et al.*, 2007; *Korth et al.*, 2012]. Our statistical results do not contradict the findings from previous kinetic hybrid simulations, including the prediction of a closed-belt proton population encircling the planet near the equator. This feature was most evident in simulations with low and constant solar wind pressure [*Trávníček et al.*, 2007] or northward IMF conditions [*Trávníček et al.*, 2010]. Under these low-activity conditions, the magnetopause standoff distance, and the size of the magnetosphere in general, is larger than encountered for the average magnetosphere. Mercury's space environment is highly dynamic [*Slavin et al.*, 2007, 2010a, 2010b, 2012; *DiBraccio et al.*, 2013], and solar wind dynamic pressure and IMF magnitude and direction, which control magnetospheric configuration and dynamics, vary on short timescales. In contrast, solar wind conditions that are stable over prolonged periods of time, as assumed for the simulations cited above, are rarely observed. Thus, it is not surprising that the observed average distribution, which reflects the full range of dynamic conditions, deviates from the simulation results.

Finally, structure in the nightside plasma sheet with invariant latitude is unmistakable in the FIPS proton data. At lower altitudes, the plasma populations observed by FIPS and inferred from the magnetic field data on the descending orbit leg show a pronounced north-south asymmetry (cf. Figures 3a, 8a, and 9a). On the descending leg of the orbit, the nighttime northern hemisphere proton fluxes are observed in two latitudinal bands, a few degrees wide in invariant latitude separated by a gap of 10° to 20° (cf. Figure 8a). This double-banded structure is also recognizable in the distribution of the proton pressure (Figure 9a). The southern hemisphere distribution exhibits higher fluxes and has no gap. Observations from the ascending orbit leg do not exhibit this asymmetry but do not sample as low in invariant latitude owing to the higher altitudes on the ascending leg of the MESSENGER orbit during the time the data were acquired for this study.

There are several features of the invariant latitude distributions that provide clues to the origin of this north-south asymmetry in the observed proton fluxes and pressure. First, we note that the high proton counts and pressures in the southern hemisphere of the descending leg data (Figure 8a) occur on closed field lines, that is, equatorward of the white lines denoting the open-closed boundary. In the north, the increase in proton fluxes with increasing λ on the nightside occurs near the open-closed boundary. The midlatitude region featuring enhanced proton fluxes is largely contained within the closed field line region, where these particles bounce along the field lines between hemispheres and can be at least partially trapped. On the other hand, the plasma population on open field lines, which do not support trapping, is tenuous. Second, the ascending orbit leg observations (Figure 8b) exhibit comparable proton fluxes near the open-closed boundary in both the north and south. Third, the northern hemisphere fluxes on the ascending leg are higher than they are on the descending leg even though the orbits on average sample the same field lines near the open-closed boundary. In the south, in contrast, the ascending leg fluxes are essentially the same as those on the descending leg at the same λ and local time. Thus, the asymmetry is prevalent primarily or only in the

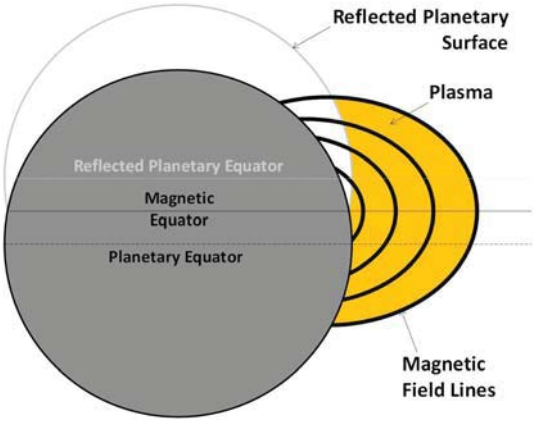

Figure 11. Formation of a plasma void at low altitudes in the northern hemisphere of the planet (filled grey circle) with the planetary and magnetic equators marked by dashed and solid black lines, respectively. The heavy black lines indicate a set of closed field lines originating from a spin-axis-aligned dipole offset northward as illustrated. See text for details.

descending node observations, and there is a difference in the flux magnitude on the same closed field lines when observed on the ascending and descending orbit legs in the northern hemisphere.

The observations therefore suggest that something must be distinctive about the region of space traversed by the spacecraft in the northern hemisphere on the descending orbit leg such that the proton fluxes are reduced relative to their levels elsewhere on the same closed field lines. The red line in Figure 8a in the northern hemisphere shows the boundary where, on average, the local magnetic field magnitude observed in the northern hemisphere is equal to the southern hemisphere surface magnetic field magnitude as calculated from either the best-fit or modified *Alexeev et al.* [2010] models. (Both versions of the model give the same result for this calculation since the thickness of the cross-tail current has little effect on the model field at the planetary surface). For λ northward of the red line, the local magnetic field at the MESSENGER spacecraft is greater than the southern hemisphere surface field on the same field line. For λ southward of the red line, in contrast, the in situ magnetic field is lower than the conjugate southern hemisphere surface field. Remarkably, the boundary between in situ magnetic fields higher and lower than the conjugate southern hemisphere surface field very closely marks the equatorward band of enhanced fluxes in the northern hemisphere descending-leg distribution. Where the in situ magnetic field exceeds the conjugate southern hemisphere surface field, the fluxes are depressed.

This result motivates the interpretation illustrated in Figure 11. Charged particles on these magnetic field lines will gyrate about the field line and bounce between mirror points depending on the pitch angle $\sin^2\alpha_{min} = B_{eq}/B_m$, where the subscripts on field magnitude denote the magnetic equator and the mirror point, respectively [e.g., *Baumjohann and Treumann*, 1997]. Particles with pitch angle $\alpha_{min} = 90°$ mirror at the equator. On any closed field line, the minimum pitch angle, α_{min}, of particles that do not encounter the planetary surface is given by $\sin^2\alpha_{min} = B_{eq}/B_{surf,S}$ where $B_{surf,S}$ is the field magnitude at the southern hemisphere surface on the field line. The projection of this surface in the northern hemisphere is shown by the grey circle labeled "reflected planetary surface" and is obtained by reflecting the planetary surface about the magnetic equator. The portions of field lines in the northern hemisphere that lie below this surface are populated only by particles for which the mirror points lie below the surface in the southern hemisphere. Thus, the region occupied by trapped plasma lies above this surface and is indicated by orange shading in the figure. We therefore interpret the region of depressed fluxes in the northern hemisphere on the descending orbit leg as indicating passage of the spacecraft through the void region of closed field lines, below the population of stably trapped plasma. Protons in this region are observed either on their first bounce after entering the closed field region or as they bounce from the southern hemisphere to the north after being pitch-angle scattered into the southern hemisphere loss cone. Thus, one expects much lower fluxes in this region and perhaps an increase of flux near the open-closed field line boundary, as observed. The result implies that plasma sheet precipitation occurs primarily in the southern hemisphere and that this loss process produces a substantial loss cone in the plasma sheet proton distribution, which in turn will promote local ion plasma-wave instabilities, which are also observed [*Boardsen et al.*, 2009, 2012].

5. Summary

We have extended the analysis of the plasma distribution in Mercury's magnetosphere by combining direct observations of protons by the FIPS sensor with total plasma pressures inferred from observations of magnetic pressure deficits by the Magnetometer both on the MESSENGER spacecraft in orbit about Mercury.

The distribution of proton fluxes and pressures compares favorably with regions exhibiting depressions in the magnetic field associated with the presence of plasma. On average, the magnitudes of the magnetic pressure deficit and of the proton pressure compare well, although the plasma pressure may differ for individual events by as much as a factor of ~3. The FIPS proton distributions also provide better statistics in regions where the plasma is more tenuous or where magnetic depressions are difficult to identify, such as near the dayside equator. Moreover, the proton data reveal features not previously identified, including very low fluxes in the dayside closed-field-line region, consistent with the absence of closed drift paths at Mercury, and an enhanced plasma population near the magnetopause flanks resulting from direct entry of magnetosheath plasma into the low-latitude boundary layer of the magnetosphere. The fluxes of protons at the dawn flank are markedly higher than at the dusk flank, suggesting that direct entry is greater at dawn, perhaps due to a corresponding asymmetry in Kelvin-Helmholtz wave-driven diffusion. Finally, the plasma observations also confirm the north-south asymmetry of the planetary dipole magnetic field, which is evident in the proton data via a depression in fluxes on closed field lines in the northern hemisphere when the spacecraft samples locations where the local field exceeds the conjugate southern hemisphere surface field. This outcome implies that particle loss to the southern hemisphere surface during bounce motion in Mercury's offset dipole magnetic field is a prominent loss mechanism for charged particles in the plasma sheet.

Acknowledgments

The MESSENGER project is supported by the NASA Discovery Program under contracts NAS5-97271 to The Johns Hopkins University Applied Physics Laboratory and NASW-00002 to the Carnegie Institution of Washington.

Masaki Fujimoto thanks the reviewers for their assistance in evaluating this paper.

References

Alexeev, I. I., et al. (2010), Mercury's magnetospheric magnetic field after the first two MESSENGER flybys, *Icarus*, *209*, 23–39, doi:10.1016/j.icarus.2010.01.024.

Anderson, B. J., M. H. Acuña, D. A. Lohr, J. Scheifele, A. Raval, H. Korth, and J. A. Slavin (2007), The Magnetometer instrument on MESSENGER, *Space Sci. Rev.*, *131*, 417–450.

Anderson, B. J., C. L. Johnson, H. Korth, M. E. Purucker, R. M. Winslow, J. A. Slavin, S. C. Solomon, R. L. McNutt Jr., J. M. Raines, and T. H. Zurbuchen (2011), The global magnetic field of Mercury from MESSENGER orbital observations, *Science*, *333*, 1859–1862.

Anderson, B. J., C. L. Johnson, H. Korth, R. M. Winslow, J. E. Borovsky, M. E. Purucker, J. A. Slavin, S. C. Solomon, M. T. Zuber, and R. L. McNutt Jr. (2012), Low-degree structure in Mercury's planetary magnetic field, *J. Geophys. Res.*, *117*, E00l12, doi:10.1029/2012je004159.

Andrews, G. B., et al. (2007), The Energetic Particle and Plasma Spectrometer instrument on the MESSENGER spacecraft, *Space Sci. Rev.*, *131*, 523–556, doi:10.1007/s11214-007-9272-5.

Axford, W. I. (1964), Viscous interaction between the solar wind and the Earth's magnetosphere, *Planet. Space Sci.*, *12*, 45–54, doi:10.1016/0032-0633(64)90067-4.

Baumjohann, W., and R. A. Treumann (1997), *Basic Space Plasma Physics*, 329 pp., Imperial College Press, London.

Baumjohann, W., G. Paschmann, and C. A. Cattell (1989), Average plasma properties in the central plasma sheet, *J. Geophys. Res.*, *94*, 6597–6606, doi:10.1029/Ja094ia06p06597.

Boardsen, S. A., B. J. Anderson, M. H. Acuña, J. A. Slavin, H. Korth, and S. C. Solomon (2009), Narrow-band ultra-low-frequency wave observations by MESSENGER during its January 2008 flyby through Mercury's magnetosphere, *Geophys. Res. Lett.*, *36*, L01104, doi:10.1029/2008GL036034.

Boardsen, S. A., T. Sundberg, J. A. Slavin, B. J. Anderson, H. Korth, S. C. Solomon, and L. G. Blomberg (2010), Observations of Kelvin-Helmholtz waves along the dusk-side boundary of Mercury's magnetosphere during MESSENGER's third flyby, *Geophys. Res. Lett.*, *37*, L12101, doi:10.1029/2010gl043606.

Boardsen, S. A., J. A. Slavin, B. J. Anderson, H. Korth, D. Schriver, and S. C. Solomon (2012), Survey of coherent ~1 Hz waves in Mercury's inner magnetosphere from MESSENGER observations, *J. Geophys. Res.*, *117*, A00M05, doi:10.1029/2012ja017822.

Büchner, J., and L. M. Zelenyi (1989), Regular and chaotic charged-particle motion in magnetotail-like field reversals, 1. Basic theory of trapped motion, *J. Geophys. Res.*, *94*, 11,821–811,842.

Delcourt, D. C., S. Grimald, F. Leblanc, J. J. Berthelier, A. Millilo, A. Mura, S. Orsini, and T. E. Moore (2003), A quantitative model of the planetary Na^+ contribution to Mercury's magnetosphere, *Ann. Geophys.*, *21*, 1723–1736.

DiBraccio, G. A., J. A. Slavin, S. A. Boardsen, B. J. Anderson, H. Korth, T. H. Zurbuchen, J. M. Raines, D. N. Baker, R. L. McNutt, and S. C. Solomon, (2013), MESSENGER observations of magnetopause structure and dynamics at Mercury, *J. Geophys. Res. Space Physics*, *118*, 997–1008, doi:10.1029/2012JA017959.

Dungey, J. W. (1961), Interplanetary magnetic field and auroral zones, *Phys. Rev. Lett.*, *6*, 47–48.

Eastman, T. E., L. A. Frank, and C. Y. Huang (1985), The boundary-layers as the primary transport regions of the Earth's magnetotail, *J. Geophys. Res.*, *90*, 9541–9560, doi:10.1029/Ja090ia10p09541.

Fairfield, D. H., A. Otto, T. Mukai, S. Kokubun, R. P. Lepping, J. T. Steinberg, A. J. Lazarus, and T. Yamamoto (2000), Geotail observations of the Kelvin-Helmholtz instability at the equatorial magnetotail boundary for parallel northward fields, *J. Geophys. Res.*, *105*, 21,159–21,173, doi:10.1029/1999ja000316.

Feldman, W. C., J. R. Asbridge, S. J. Bame, and J. T. Gosling (1978), Long-term variations of selected solar-wind properties—IMP 6, 7, and 8 results, *J. Geophys. Res.*, *83*, 2177–2189, doi:10.1029/Ja083ia05p02177.

Fuselier, S. A., E. G. Shelley, and O. W. Lennartsson (1997), Solar wind composition changes across the Earth's magnetopause, *J. Geophys. Res.*, *102*, 275–283, doi:10.1029/96ja02355.

Fuselier, S. A., R. C. Elphic, and J. T. Gosling (1999), Composition measurements in the dusk flank magnetosphere, *J. Geophys. Res.*, *104*, 4515–4522, doi:10.1029/1998ja900137.

Gershman, D. J., J. A. Slavin, J. M. Raines, T. H. Zurbuchen, B. J. Anderson, H. Korth, D. N. Baker, and S. C. Solomon (2013), Magnetic flux pile-up and plasma depletion in Mercury's subsolar magnetosheath, *J. Geophys. Res. Space Physics*, *118*, 7181–7299, doi:10.1002/2013JA019244.

Glassmeier, K. H., and J. Espley (2006), ULF waves in planetary magnetospheres, in *Magnetospheric ULF Waves: Synthesis and New Directions*, edited by K. Takahashi et al., pp. 341–359, AGU, Washington, D. C.

Goertz, C. K., and W. Baumjohann (1991), On the thermodynamics of the plasma sheet, *J. Geophys. Res.*, *96*, 20,991–20,998, doi:10.1029/91ja02128.

Herčík, D., P. M. Trávníček, J. R. Johnson, E. H. Kim, and P. Hellinger (2013), Mirror mode structures in the asymmetric Hermean magnetosheath: Hybrid simulations, *J. Geophys. Res. Space Physics*, *118*, 405–417, doi:10.1029/2012ja018083.

Imber, S. M., J. A. Slavin, S. A. Boardsen, B. J. Anderson, H. Korth, D. N. Baker, R. L. McNutt Jr., and S. C. Solomon (2013), MESSENGER observations of large dayside flux transfer events: Do they drive Mercury's substorm cycle?, Abstract P12B-07, presented at 2013 Fall Meeting, AGU, San Francisco, Calif., 9–13 Dec.

Johnson, C. L., et al. (2012), MESSENGER observations of Mercury's magnetic field structure, *J. Geophys. Res.*, *117*, E00l14, doi:10.1029/2012je004217.

Korth, H., B. J. Anderson, J. M. Raines, J. A. Slavin, T. H. Zurbuchen, C. L. Johnson, M. E. Purucker, R. M. Winslow, S. C. Solomon, and R. L. McNutt Jr. (2011), Plasma pressure in Mercury's equatorial magnetosphere derived from MESSENGER Magnetometer observations, *Geophys. Res. Lett.*, *38*, L22201, doi:10.1029/2011GL049451.

Korth, H., B. J. Anderson, C. L. Johnson, R. M. Winslow, J. A. Slavin, M. E. Purucker, S. C. Solomon, and R. L. McNutt (2012), Characteristics of the plasma distribution in Mercury's equatorial magnetosphere derived from MESSENGER Magnetometer observations, *J. Geophys. Res.*, *117*, A00M07, doi:10.1029/2012ja018052.

Lennartsson, W. (1992), A scenario for solar-wind penetration of Earth's magnetic tail based on ion composition data from the ISEE-1 spacecraft, *J. Geophys. Res.*, *97*, 19,221–19,238, doi:10.1029/92ja01604.

Lennartsson, W., and E. G. Shelley (1986), Survey of 0.1-keV/e to 16-keV/e plasma sheet ion composition, *J. Geophys. Res.*, *91*, 3061–3076, doi:10.1029/Ja091ia03p03061.

Nagano, H. (1979), Effect of finite ion Larmor radius on the Kelvin-Helmholtz instability of the magnetopause, *Planet. Space Sci.*, *27*, 881–884.

Nakamura, T. K. M., H. Hasegawa, and I. Shinohara (2010), Kinetic effects on the Kelvin-Helmholtz instability in ion-to-magnetohydrodynamic scale transverse velocity shear layers: Particle simulations, *Phys. Plasmas*, *17*, 042119, doi:10.1063/1.3385445.

Ness, N. F. (1979), The magnetosphere of Mercury, in *Solar System Plasma Physics*, vol. II, edited by C. F. Kennel, L. J. Lanzerotti, and E. N. Parker, pp. 185–206, North-Holland Company, Amsterdam, Netherlands.

Otto, A., and D. H. Fairfield (2000), Kelvin-Helmholtz instability at the magnetotail boundary: MHD simulation and comparison with Geotail observations, *J. Geophys. Res.*, *105*, 21,175–21,190, doi:10.1029/1999ja000312.

Paral, J., and R. Rankin (2013), Dawn-dusk asymmetry in the Kelvin-Helmholtz instability at Mercury, *Nature Commun.*, *4*, 1645, doi:10.1038/Ncomms2676.

Parker, E. N. (1957), Sweet's mechanism for merging magnetic fields in conducting fluids, *J. Geophys. Res.*, *62*, 509–520, doi:10.1029/JZ062i004p00509.

Petschek, H. E. (1964), Magnetic field annihilation, in *Physics of Solar Flares*, Spec. Pub. 50, edited by W. N. Ness, pp. 425–439, National Aeronautics and Space Administration, Washington, D. C.

Raines, J. M., J. A. Slavin, T. H. Zurbuchen, G. Gloeckler, B. J. Anderson, D. N. Baker, H. Korth, S. M. Krimigis, and R. L. McNutt Jr. (2011), MESSENGER observations of the plasma environment near Mercury, *Planet. Space Sci.*, *59*, 2004–2015, doi:10.1016/j.pss.2011.02.004.

Raines, J. M., et al. (2013), Distribution and compositional variations of plasma ions in Mercury's space environment: The first three Mercury years of MESSENGER observations, *J. Geophys. Res. Space Physics*, *118*, 1604–1619, doi:10.1029/2012ja018073.

Roederer, J. G. (1970), *Dynamics of Geomagnetically Trapped Radiation*, Springer, New York.

Russell, C. T., D. N. Baker, and J. A. Slavin (1988), The magnetosphere of Mercury, in *Mercury*, edited by F. Vilas, C. R. Chapman, and M. S. Matthews, pp. 514–561, University of Arizona Press, Tucson, Ariz.

Slavin, J. A., et al. (2007), MESSENGER: Exploring Mercury's magnetosphere, *Space Sci. Rev.*, *131*, 133–160.

Slavin, J. A., et al. (2010a), MESSENGER observations of extreme loading and unloading of Mercury's magnetic tail, *Science*, *329*, 665–668, doi:10.1126/science.1188067.

Slavin, J. A., et al. (2010b), MESSENGER observations of large flux transfer events at Mercury, *Geophys. Res. Lett.*, *37*, L02105, doi:10.1029/2009gl041485.

Slavin, J. A., et al. (2012), MESSENGER observations of a flux-transfer-event shower at Mercury, *J. Geophys. Res.*, *117*, A00M06, doi:10.1029/2012ja017926.

Solomon, S. C., et al. (2001), The MESSENGER mission to Mercury: Scientific objectives and implementation, *Planet. Space Sci.*, *49*, 1445–1465.

Spence, H. E., M. G. Kivelson, R. J. Walker, and D. J. McComas (1989), Magnetospheric plasma pressures in the midnight meridian—Observations from 2.5 to 35 R_E, *J. Geophys. Res.*, *94*, 5264–5272, doi:10.1029/Ja094ia05p05264.

Sundberg, T., S. A. Boardsen, J. A. Slavin, L. G. Blomberg, and H. Korth (2010), The Kelvin-Helmholtz instability at Mercury: An assessment, *Planet. Space Sci.*, *58*, 1434–1441, doi:10.1016/j.pss.2010.06.008.

Sundberg, T., S. A. Boardsen, J. A. Slavin, L. G. Blomberg, J. A. Cumnock, S. C. Solomon, B. J. Anderson, and H. Korth (2011), Reconstruction of propagating Kelvin-Helmholtz vortices at Mercury's magnetopause, *Planet. Space Sci.*, *59*, 2051–2057, doi:10.1016/j.pss.2011.05.008.

Sundberg, T., S. A. Boardsen, J. A. Slavin, B. J. Anderson, H. Korth, T. H. Zurbuchen, J. M. Raines, and S. C. Solomon (2012), MESSENGER orbital observations of large-amplitude Kelvin-Helmholtz waves at Mercury's magnetopause, *J. Geophys. Res.*, *117*, A04216, doi:10.1029/2011ja017268.

Terasawa, T., et al. (1997), Solar wind control of density and temperature in the near-Earth plasma sheet: WIND/GEOTAIL collaboration, *Geophys. Res. Lett.*, *24*, 935–938, doi:10.1029/96gl04018.

Trávníček, P. M., P. Hellinger, and D. Schriver (2007), Structure of Mercury's magnetosphere for different pressure of the solar wind: Three dimensional hybrid simulations, *Geophys. Res. Lett.*, *34*, L05104, doi:10.1029/2006GL028518.

Trávníček, P. M., D. Schriver, P. Hellinger, D. Herčík, B. J. Anderson, M. Sarantos, and J. A. Slavin (2010), Mercury's magnetosphere-solar wind interaction for northward and southward interplanetary magnetic field: Hybrid simulation results, *Icarus*, *209*, 11–22, doi:10.1016/j.icarus.2010.01.008.

Wing, S., and P. T. Newell (1998), Central plasma sheet ion properties as inferred from ionospheric observations, *J. Geophys. Res.*, *103*, 6785–6800.

Winslow, R. M., C. L. Johnson, B. J. Anderson, H. Korth, J. A. Slavin, M. E. Purucker, and S. C. Solomon (2012), Observations of Mercury's northern cusp region with MESSENGER's Magnetometer, *Geophy. Res. Lett.*, *39*, L08112, doi:10.1029/2012GL051472.

Winslow, R. M., B. J. Anderson, C. L. Johnson, J. A. Slavin, H. Korth, M. E. Purucker, D. N. Baker, and S. C. Solomon (2013), Mercury's magnetopause and bow shock from MESSENGER Magnetometer observations, *J. Geophys. Res. Space Physics*, *118*, 2213–2227, doi:10.1002/jgra.50237.

Zurbuchen, T. H., et al. (2011), MESSENGER observations of the spatial distribution of planetary ions near Mercury, *Science*, *333*, 1862–1865, doi:10.1126/science.1211302.